Dynamic Nuclear Polarization of Metal-Doped Oxide Glasses: A Test of the Generality of Paramagnetic Metal Polarizing Agents

Alexander L. Paterson,[1] Frédéric A. Perras,[1]* Matthew F. Besser,[1] Marek Pruski[1,2]*

[1]US DOE, Ames Laboratory, Ames, IA 50011

[2]Department of Chemistry, Iowa State University, Ames, IA 50011

Abstract.
Nuclear magnetic resonance (NMR) spectroscopy can provide unique, atomic-level, insights into the structure and dynamics of materials, but applications are impeded by its intrinsically low sensitivity. Dynamic nuclear polarization (DNP) is poised to overcome this limitation, and indeed has revolutionized the study of surfaces; however, the current approaches are ill-suited for bulk solids. One potential pathway towards the hyperpolarization of bulk solids by DNP is through the inclusion of paramagnetic metal ions that can serve as polarizing agents. In this work, we compared the relative performance of two such dopants, Mn^{2+} and Gd^{3+}, in three series of oxide glasses having chemical environments representative of those found in other crystalline and amorphous solids. In our studies, Gd^{3+} outperformed Mn^{2+}, consistently providing more than one order of magnitude greater time savings. We attributed this difference mainly to its lack of hyperfine interaction.

Graphical Abstract.
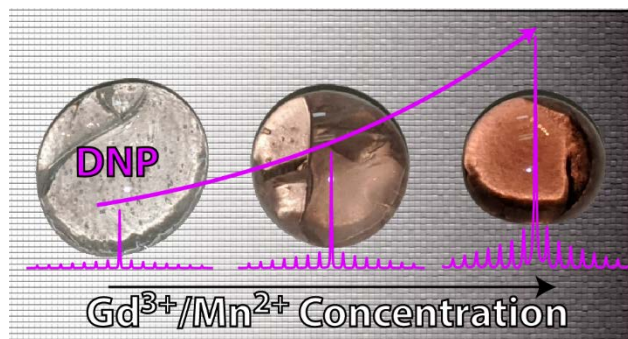
1. Introduction.

Solid-state nuclear magnetic resonance (SSNMR) spectroscopy is a powerful technique for investigating the atomic-scale structure of both organic and inorganic solids. It nevertheless suffers from intrinsically low sensitivity, which is often exacerbated by low natural isotopic abundances, small nuclear magnetic moments, low-concentration environments, line broadening, and other factors. One way to compensate for the small magnetic moments of nuclei is to dramatically enhance their magnetization through a transfer of polarization from the much more magnetic electrons; an approach called dynamic nuclear polarization (DNP). This can be achieved by irradiating unpaired electrons at or near their electron paramagnetic resonance (EPR) frequency with high-powered microwaves.[1,2] The maximum enhancement obtainable though DNP corresponds to the ratio of the gyromagnetic ratios of the electron and the nucleus; for ^{29}Si this ratio is 3300 which translates to even higher potential time savings.[3] Because of these large enhancements, high-field DNP has revolutionized the study of surfaces and interfaces, where sites are generally very dilute,[4,5] and indeed has been applied to a wide range of inorganic systems, including heterogeneous catalysts, battery materials, and nanomaterials.[6-12]

To perform DNP, unpaired electrons must first be introduced into the sample. Typically, this is achieved via incipient wetness impregnation with persistent organic radicals. While this approach dramatically enhances signals from the nuclei located at or near the surface, it has little effect on the bulk of the material,[5,12] unless spin diffusion can transport magnetization from the surface to the target nuclei of interest.[13-16] Several recent studies highlighted the need for innovative means to reproducibly hyperpolarize the bulk of materials. In the case of inorganic materials, Björgvinsdóttir and coworkers have implemented a strategy relying on spin diffusion among weakly magnetic nuclei from the surface. This technique is best suited for applications to materials with long spin-lattice relaxation time constants (T_1) and relatively high spin densities.[17-19] Radicals have been introduced into solid samples via electrical discharge with some success.[20,21] Alternatively, Carnahan and coworkers obtained remarkable DNP enhancements, surpassing 400 in fused quartz, by using γ-ray radiation to introduce radical defects to the material's interior.[22]

Another potential source of unpaired electrons is paramagnetic metal ions. Indeed, Gd^{3+}, Mn^{2+}, Cr^{3+}, and Fe^{3+} have been explored as endogenous polarizing agents for high-field magic angle spinning (MAS) DNP NMR of inorganic materials.[23-29] The most recent studies by Leskes and coworkers demonstrated impressive enhancements achieved in the spinel phase of LTO ($Li_4Ti_5O_{12}$), first by doping with Mn^{2+}, which allowed for the natural abundance detection of ^{17}O,[30] and then by introducing Fe^{3+}, which also served to improve the properties of LTO.[31,32] Previous work, however, has focused on studying cations that occupy crystalline, or ligated, sites of high symmetry, so as to limit their zero field splitting and g anisotropy.[25,30-33] It remains to be seen whether these cations will yield consistently high DNP enhancements in a wider array of materials. Here, we compared the DNP performance of Gd^{3+} and Mn^{2+} dopants in several oxide glasses, which are representative of both the chemical environments generally found in oxide materials, as well as environments with low symmetry.

To this end, we prepared Mn^{2+}- and Gd^{3+}-doped lithium silicate, lithium borate, and zinc phosphate glasses with varied dopant concentrations, and measured their ^7Li, ^{11}B, ^{29}Si, and ^{31}P NMR spectra, as well as DNP field sweep enhancement profiles, to compare the sensitivity enhancements obtained from DNP using either cation.

2. Methods.

2.1. Sample Preparation. Lithium silicate, lithium borate, and zinc phosphate glasses were doped with varying amounts of either Gd_2O_3 ($\geq$99.99% trace metals basis, Sigma Aldrich) or MnO (99%, Strem Chemicals). The targeted compositions were $40Li_2O-60SiO_2$, $41.5Li_2O-58.5B_2O_3$, and $64ZnO-36P_2O_5$, with

the proportions given on a molar basis. The sample series are labelled herein as LiSi$_{xM}$, LiB$_{xM}$, and ZnP$_{xM}$ for the lithium silicate, lithium borate, and zinc phosphate glasses, respectively, where x indicates the millimolar metal ion dopant concentration and M is either Gd^{3+} or Mn^{2+}. Dopant concentrations ranged from 3.5 mM to 100 mM for the LiSi and LiB series, and from 9 to 729 mM for the ZnP series. Concentrations were calculated using batched compositions and densities obtained from the literature.[34,35,36]

The LiSi series was synthesized using Li$_2$CO$_3$ (99.997% trace metals basis, Sigma Aldrich) and SiO$_2$ ($\geq$99.997% trace metals basis, Sigma Aldrich). Appropriately weighed amounts of Li$_2$O$_3$, SiO$_2$, and dopant were thoroughly ground in a porcelain mortar and pestle, placed in platinum crucibles, and transferred to a 1500 °C furnace in air for approximately 1 h.

The LiB was synthesized using Li$_2$CO$_3$ (99.997% trace metals basis, Sigma Aldrich) and B$_2$O$_3$. The B$_2$O$_3$ was produced by heating H$_3$BO$_3$ ($\geq$99.95% ACS reagent grade, Sigma Aldrich) in a platinum crucible in air at 400 °C for several hours. Appropriately weighed amounts of Li$_2$CO$_3$, B$_2$O$_3$, and dopant were thoroughly ground in a porcelain mortar and pestle, then transferred to platinum crucibles. The crucibles were placed in a room-temperature furnace, brought to 1000 °C at a rate of 20 °C min^{-1}, and held at 1000 °C for approximately 30 min.

The ZnP series was synthesized using NH$_4$H$_2$PO$_4$ ($\geq$98% ACS reagent grade, Sigma Aldrich) and ZnO ($\geq$99% ACS reagent grade, Sigma Aldrich). Appropriately weighed amounts of Li$_2$O$_3$, SiO$_2$, and dopant were thoroughly ground in a porcelain mortar and pestle and placed in corundum crucibles. The crucibles were placed in a room-temperature furnace, brought to 400 °C, and held at 400 °C for about 12 h. The furnace was then brought to 1000 °C at a rate of 20 °C min^{-1} and held at 1000 °C for 1 h. Synthesis in corundum crucibles may introduce some Al$_2$O$_3$ contamination to the glasses, but this contamination should be consistent across the sample series. As we are not probing specific structural features, mechanical properties, or thermal properties, we do not anticipate this contamination to affect the conclusions of our study.

All glasses were quenched on a thick copper plate to avoid crystallization and stored in a desiccator prior to analysis. The LiB samples were quenched by pressing the poured melt between two copper plates, as it had a tendency to crystallize. These procedures are expected to promote a homogeneous metal dopant distribution. This was verified by monitoring the dependence of the T_1 relaxation times on the dopant concentration, which is expected to follow a $[M]^{-1}$ dependence in the presence of spin diffusion[37,38] and a $[M]^{-2}$ dependence in its absence.[39,40] In Figures 3, 4, and 6 all glasses followed approximately a $[M]^{-1}$ dependence (see also Table S1) confirming that the metal dopants were indeed homogeneously distributed in the glasses. Note that there is some variation in the T_1 values for the lowest-doped glasses, presumably due to the larger impact that minute paramagnetic impurities have on those samples (see Figure S12).

2.2. NMR Spectroscopy. DNP NMR experiments were performed using a commercial 264 GHz/400 MHz Bruker AVANCE III DNP NMR spectrometer and a 3.2-mm low-temperature magic-angle-spinning (MAS) probe equipped with sapphire rotors and operated at a temperature of *ca*. 110 K. Approximately 16 W of microwave power was used, unless otherwise stated, with MAS rates of 10 kHz for ^{7}Li, ^{11}B and ^{29}Si or 12.5 kHz for ^{31}P experiments. All spectra were collected using Bloch decays, with excitation pulse durations of 1 µs for ^{7}Li, 0.5 µs for ^{11}B, and 3 µs for ^{29}Si and ^{31}P nuclei. The spin-lattice relaxation times (T_1) were determined for each sample using a saturation recovery experiment with 100 presaturation pulses. Most T_1 values were determined by fitting the saturation recovery data with an exponential function. One of the ^{31}P and all of the ^{29}Si build-up curves were found to be multiexponential and were instead fit to stretched exponentials $(\exp(t/T_1')^\beta)$.[41] The use of a stretched exponential is consistent with a distribution of T_1 values. The reported mean T_1 values are determined by the equation $T_1 = (T_1'/\beta) \times \Gamma(1/\beta)$, where Γ is

the Gamma function.[42,43] The T_1' and the β values for the relevant samples are reported in Table S2 in the Supporting Information. The DNP enhancement factors, $\varepsilon_{on/off}$, were determined with relaxation delays set to $1.3T_1$. Small background signals were observable in the ^{11}B and ^{29}Si spectra; these were subtracted from spectra of samples prior to analysis. All spectra were collected at the field position corresponding to the maximum DNP enhancement for a given dopant/nucleus pair. θ values were measured as the integrated intensity of the entire spectrum relative to that in the undoped sample in the absence of microwaves. The NMR experiments were conducted using samples with known masses to which all intensity-based quantities were normalized.

3. Results and Discussion.

Generally, four parameters influence the relative sensitivity of a DNP NMR experiment, relative to an experiment performed in the absence of DNP on the same hardware: changes in T_1 relaxation relative to an undoped sample ($\chi = T_{1,doped}/T_{1,undoped}$), signal losses due to paramagnetic effects (given by the contribution factor, θ, which is the fraction of spins that remains observable following the introduction of radicals), relative differences in linewidths due to paramagnetic broadening, and the DNP enhancement factor, $\varepsilon_{on/off}$.[44] Note that contained in θ are the bleaching effects and a contribution from cross-effect induced depolarization, if it is present, which leads to a reduction in nuclear magnetization when the EPR resonance is not irradiated.[45,46] These four parameters depend intimately on the properties of the electrons (T_{1e}, T_{2e}, g tensor, hyperfine interactions, and zero field splitting) as well as those of the nuclei, their distribution, and hardware-specific factors such as microwave power and magnetic field. Disentangling all of these factors is far from trivial and is beyond the scope of this study. Given that signal to noise improves with the square root of the number of scans, the overall time savings of a DNP experiment, when compared to an analogous low-temperature experiment, can be expressed as $\varepsilon_{amp}^2 \chi^{-1}$ where ε_{amp} is simply the relative amplitude of the DNP-enhanced NMR signal in a doped sample relative to that from an undoped sample ($\varepsilon_{amp} = I_{doped} / I_{undoped}$). In the absence of increases in line broadening ε_{amp} is simply given by $\varepsilon_{on/off}\theta$ and the acceleration factor of the DNP experiment corresponds to $\varepsilon_{on/off}^2 \theta^2 \chi^{-1}$.[47] We report both the integral and amplitude time savings, $\varepsilon_{on/off}^2 \theta^2 \chi^{-1}$ and $\varepsilon_{amp}^2 \chi^{-1}$, for all samples.

3.1. DNP Mechanisms. Representative DNP field sweep profiles obtained for glasses studied in this work are shown in Figure 1a. For the Gd^{3+}-doped samples, the separation between the field sweep maxima and minima is very nearly twice the nuclear Larmor frequency (ω_N) at 9.4 T (see Table 1), which suggests that the dominant DNP process for ^{29}Si in our samples is the solid effect. However, the separation for the other nuclei is smaller, ranging from $1.46\omega_N$ to $1.58\omega_N$. This suggests that the cross-effect, which is expected to yield extrema separated by ω_N, is also significant in those samples. This difference in dominant DNP mechanisms likely originates from the ω_N^{-2} dependence of the solid effect and the ω_N^{-1} dependence of the cross-effect, given that ^{29}Si has the lowest ω_N of the studied nuclides.[2]

Table 1. Separations between the extrema in the DNP field sweep profiles for different nuclei and dopant concentrations. Separations are reported as fractions of ω_N.

Nucleus[a]	[Gd^{3+}] / mM	Separation / ω_N
^7Li	61	1.55
^{11}B	61	1.58
^{29}Si	54	1.97
^{31}P	9	1.90
	99	1.46

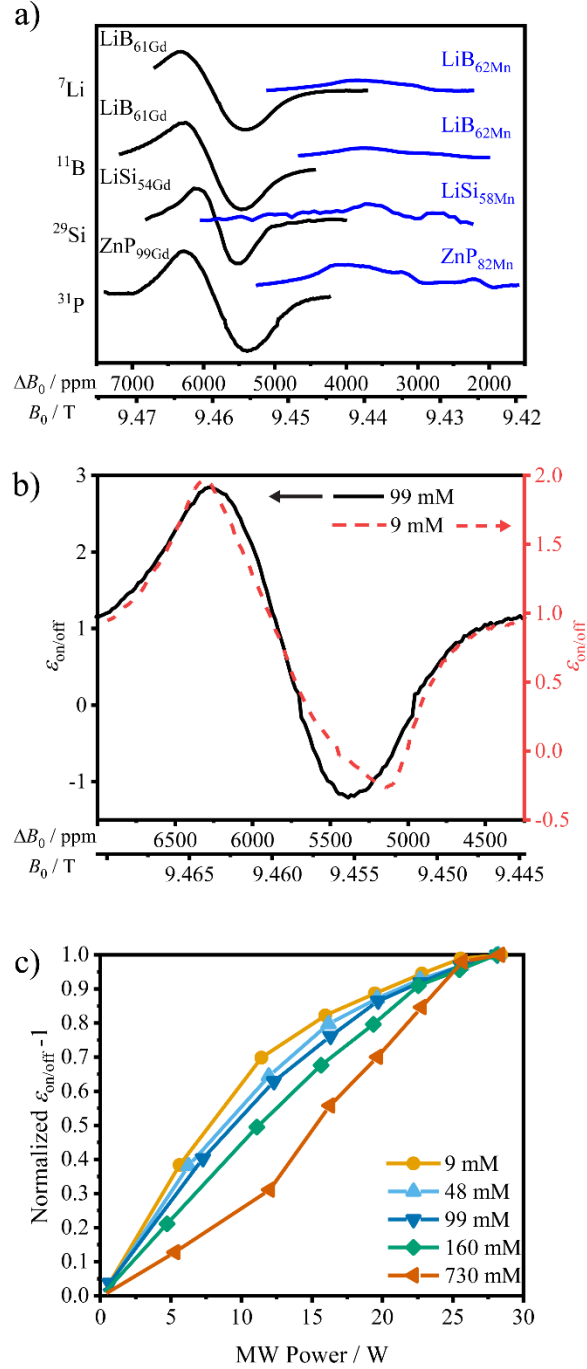[a]These correspond to the same samples listed in Figure 1.

Figure 1. a) DNP field sweep profiles of the Gd^{3+}- (black) and Mn^{2+}-doped (blue) glasses, with the nuclide being polarized indicated on the left and the specific sample used marked on the spectra. The field sweep profiles are vertically offset for clarity. b) DNP field sweep profiles of ZnP_{99Gd} (black, solid) and ZnP_{9Gd} (red, dashed). c) Normalized $\varepsilon_{on/off}$-1 values of the ZnP samples with varying Gd^{3+} dopant concentrations as a function of microwave power. The enhancement factors have been adjusted to account for microwave heating (see Figure S1).

To confirm the presence of the cross-effect, we have acquired the DNP field profiles for two different Gd^{3+} concentrations in our ZnP glasses. Given that cross-effect requires the interaction between

two Gd^{3+}-centered spins,[24] it is expected to grow in significance as the Gd^{3+} concentration is increased and the electron-electron interactions are strengthened.[26,30,48] As shown in Figure 1b and Table 1, the separation between the two extrema indeed decreased with an increase in Gd^{3+} concentration, confirming that cross-effect plays a significant role in the nuclear hyperpolarization process.

In the case of Mn^{2+}, there are six maxima and six minima, due to the hyperfine coupling to the 100% abundant ^{55}Mn nuclei (I=5/2). The highest-field maximum is expected to provide the largest enhancements, due to its minimal destructive interference with adjacent minima, and we have therefore focused on this region. The overlap between the different extrema did not enable for the evaluation of the dominant DNP mechanism for Mn^{2+}.

The effect of varying the applied microwave power was also investigated, for the Gd^{3+}-doped ZnP samples (Figure S1). While the DNP field sweep profiles in Figure 1b suggest that the DNP performance of the ZnP_{9Gd} sample is substantially driven by the solid effect, its $\varepsilon_{on/off}$ values reached a plateau at even modest applied microwave power (*ca.* 10 W, see Figure 1c). Furthermore, the power required to saturate the DNP enhancement was observed to increase with the dopant concentration, counter to the expected trend, with cross-effect generally requiring lower microwave powers due to the saturation of allowed transitions, as opposed to the forbidden transitions involved in the solid effect.[2] This is most likely caused by a decrease in the electron spin-lattice relaxation time, T_{1e}, which is expected to shorten with increasing dopant concentration.[48] More specifically, higher microwave powers are required to saturate a more rapidly relaxing EPR transition. Note that as the microwave power is increased the glass is also substantially heated by up to 45 K, as estimated from the signal intensity in the undoped sample (Figure S1a). This heating is expected to be constant across the sample series.

3.2. Sensitivity Enhancements. The spectra with the greatest time savings for each dopant/nucleus combination are shown in Figure 2. Comparing the DNP field sweep profiles (Figure 1a) and NMR spectra (Figure 2), it becomes immediately apparent that Gd^{3+} consistently outperformed Mn^{2+} by a significant margin.

3.2.1. Lithium silicate glasses. The ^{29}Si and ^{7}Li data for LiSi glasses doped with Gd^{3+} and Mn^{2+} shown in Figure 3 are representative of all glasses prepared for this study. We observed that both T_1 and θ responded similarly to changes in concentration of both paramagnetic dopants. Of all the nuclides studied, ^{29}Si had by far the longest T_1, with a value of about 4.5 h in the undoped glass. (Note that high-purity reagents, low in other paramagnetic elements such as iron, were used for the synthesis of the lithium silicate glasses.) Slow nuclear relaxation is generally beneficial for DNP, as it gives more time for polarization to be transferred over larger diffusions lengths (which depend roughly on $\sqrt{DT_1}$, where D is the spin diffusion coefficient).[17] However, due to the low abundance of ^{29}Si nuclei (4.67%) leading to low D, the long relaxation times did not result in large values of $\varepsilon_{on/off}$, which reached a maximum of 3.63 ± 0.07 when using Gd^{3+} as the paramagnetic dopant and 1.64 ± 0.03 when using Mn^{2+}; similar values were obtained with ^{7}Li, see Figure 3 and Table S4. We note that Leskes has recently shown that in cases where nuclear concentrations are low and relaxation is dominated by the paramagnetic center, the DNP enhancements should be independent of radical concentration and not require spin diffusion.[32] This was not the case in any of our glasses.

The effect of paramagnetic-induced nuclear relaxation, which was particularly dramatic in the case of ^{29}Si, is reflected in large time saving values, $\varepsilon_{on/off}^2 \theta^2 \chi^{-1}$, reaching 40 ± 20 and 27 ± 2 for ^{29}Si and ^{7}Li, respectively when using Gd^{3+}, whereas for Mn^{2+} the corresponding DNP experiments were accelerated by factors of only 4 ± 1 and 4.2 ± 0.3 (see also Tables S3 and S4). The ^{29}Si spectra did not show substantial paramagnetic broadening; however, the reverse was true for ^{7}Li, which as such had $\varepsilon_{amp}^2 \chi^{-1}$ values below

$\varepsilon_{on/off}^2\,\theta^2\chi^{-1}$ (see Figure 3b,iv). ^{29}Si nevertheless had far lower θ values than ^{7}Li, suggesting its paramagnetic broadening is hidden in the baseline.
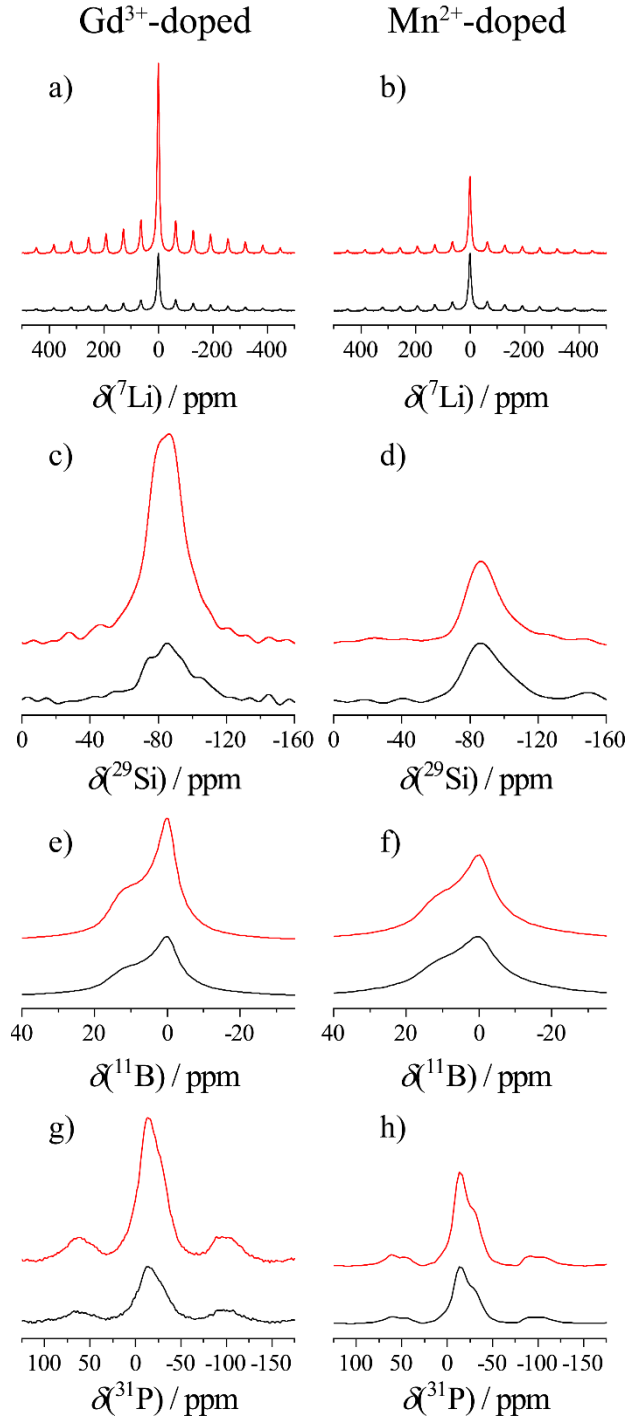

Figure 2. NMR spectra obtained on samples showing the greatest time savings, with (top, red) and without (bottom, black) microwave irradiation. Presented spectra are from the following samples: a) LiSi$_{54Gd}$; b) LiSi$_{58Mn}$; c) LiSi$_{101Gd}$; d) LiSi$_{37Mn}$; e) LiB$_{61Gd}$; f) LiB$_{111Mn}$; g) ZnP$_{161Gd}$; h) ZnP$_{43Mn}$. Spectra obtained on samples with different dopant concentrations are shown in the Supporting Information (Figures S2–S11).
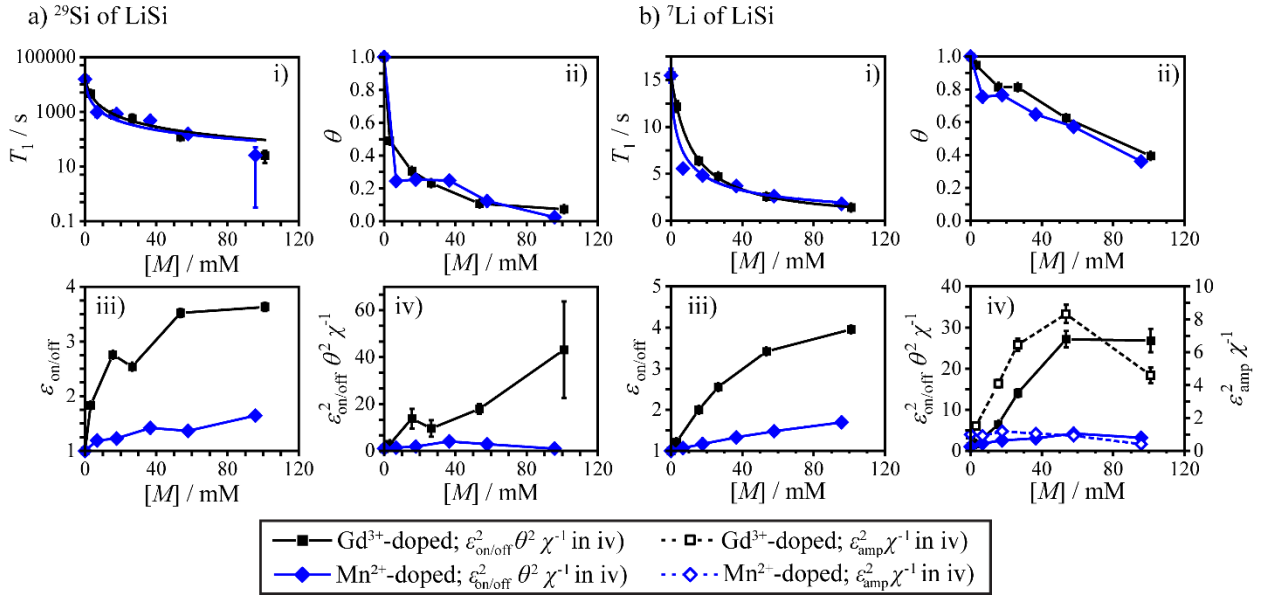
a) ^{29}Si of LiSi

i) ii) iii) iv)

b) ^{7}Li of LiSi

i) ii) iii) iv)

—■— Gd^{3+}-doped; $\varepsilon_{\mathrm{on/off}}^2 \theta^2 \chi^{-1}$ in iv) · ·□· · Gd^{3+}-doped; $\varepsilon_{\mathrm{amp}}^2 \chi^{-1}$ in iv)
—◆— Mn^{2+}-doped; $\varepsilon_{\mathrm{on/off}}^2 \theta^2 \chi^{-1}$ in iv) · ·◇· · Mn^{2+}-doped; $\varepsilon_{\mathrm{amp}}^2 \chi^{-1}$ in iv)

Figure 3. LiSi glasses: spin-lattice relaxation times T_1, contribution factors θ, DNP enhancements $\varepsilon_{\mathrm{on/off}}$, integral time savings $\varepsilon_{\mathrm{on/off}}^2 \theta^2 \chi^{-1}$, and vertical intensity time savings $\varepsilon_{\mathrm{amp}}^2 \chi^{-1}$ for a) ^{29}Si NMR and b) ^{7}Li NMR. Data from Gd^{3+}-doped glasses are presented as black squares, while data from glasses doped with Mn^{2+} are presented as blue diamonds. In iv) the white-filled symbols and dashed lines correspond to the $\varepsilon_{\mathrm{amp}}^2 \chi^{-1}$ values while the solid colors correspond to the $\varepsilon_{\mathrm{on/off}}^2 \theta^2 \chi^{-1}$ data. The ^{29}Si T_1 relaxation times are plotted on a logarithmic scale due to the wide range of relaxation times. In i), lines are a fit to the equation $\frac{1}{T_1} = \frac{1}{T_{1,\mathrm{0mM}}} + A[M]^{-B}$, where $T_{1,\mathrm{0mM}}$ is the T_1 value of the undoped sample (see Table S1). All other lines are given as a guide to the eye. The raw data are given in Tables S3 and S4 in the Supporting Information. When error bars are smaller than the symbol, they are omitted.

3.2.2. Lithium borate glasses. DNP performance was the lowest in the LiB glasses, particularly in the case of ^{11}B (Figure 4). At high dopant concentrations of *ca.* 100 mM, the ^{11}B $\varepsilon_{\mathrm{on/off}}$ values reached 2.55 ± 0.05 and 1.42 ± 0.03 with Gd^{3+} and Mn^{2+}, respectively. Microwave heating effects outpaced DNP at low dopant concentrations, leading to slight losses in sensitivity due to reductions in equilibrium Boltzmann polarization. ^{7}Li showed consistently higher $\varepsilon_{\mathrm{on/off}}$ values, which we ascribe to slower relaxation, greater gyromagnetic ratio and higher natural abundance compared to ^{11}B, which serve to improve the spin diffusion and increase the efficiency of DNP transfers. The ^{7}Li $\varepsilon_{\mathrm{on/off}}^2 \theta^2 \chi^{-1}$ time savings in Gd^{3+}-doped LiB glasses were nevertheless lower than those observed for LiSi, reaching a maximum of 26 ± 1 for Gd^{3+}. The reverse was true for the Mn^{2+}-doped samples, which is attributable to the starker change in T_1 relaxation times observed in the LiB sample series. The ^{7}Li $\varepsilon_{\mathrm{amp}}^2 \chi^{-1}$ time savings in the LiB series were also consistently lower than those in the LiSi series for both the Gd^{3+}- and Mn^{2+}-doped samples. The Mn^{2+}-doped samples showed particularly poor performance by this metric, with most samples providing less signal-per-unit time under DNP conditions than the undoped sample.

The high concentrations of paramagnetic radicals required to obtain the largest enhancements, unfortunately, consistently led to undesirable line broadening. This is perhaps best demonstrated with the ^{11}B MAS NMR spectra of the LiB glasses as a function of the Gd^{3+} dopant concentration (Figure 5). These spectra feature a sharp resonance at *ca.* 0 ppm from tetrahedral BO$_4$ units, as well as an overlapping second-

8

order quadrupolar powder pattern from trigonal BO_3 units. As can be seen, the resolution worsens as the dopant concentration is increased, with the quadrupolar features of the BO_3 resonance being broadened nearly to the point of obscurity in the sample with a 98 mM Gd^{3+} concentration.
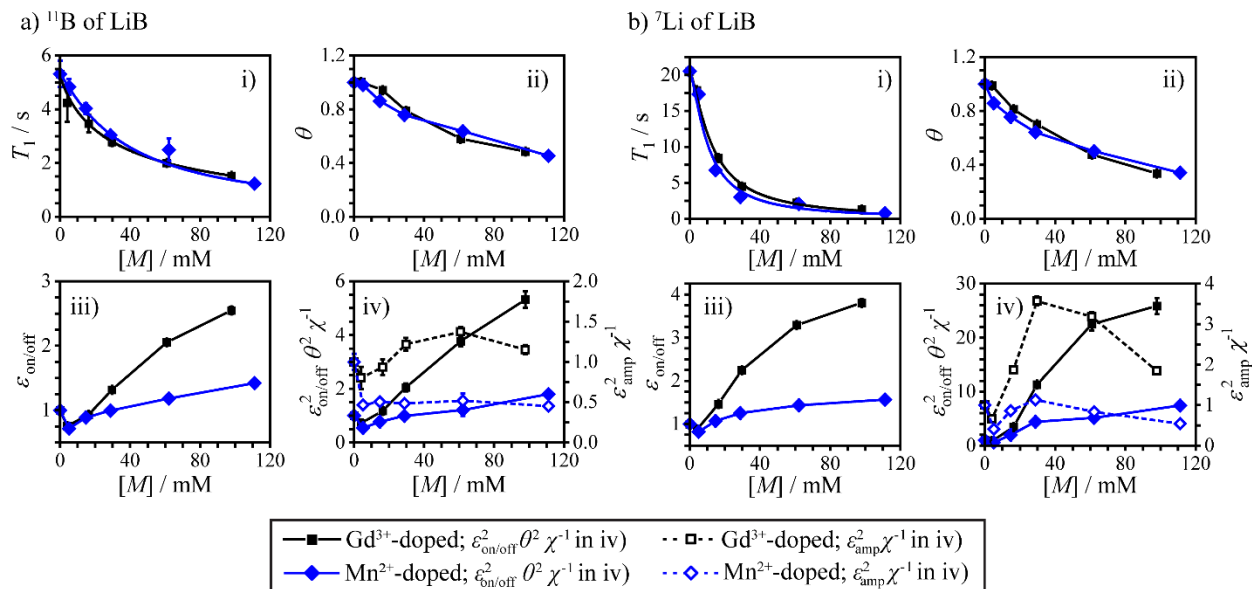

Figure 4. LiB glasses: spin-lattice relaxation times T_1, contribution factors θ, DNP enhancements $\varepsilon_{on/off}$, integral time savings $\varepsilon^2_{on/off}\,\theta^2\chi^{-1}$, and vertical intensity time savings $\varepsilon^2_{amp}\chi^{-1}$ for a) ^{11}B NMR and b) ^{7}Li NMR. Data from Gd^{3+}-doped glasses are presented as black squares, while data from glasses doped with Mn^{2+} are presented as blue diamonds. In iv) the white-filled symbols and dashed lines correspond to the $\varepsilon^2_{amp}\chi^{-1}$ values, while the solid colors correspond to the $\varepsilon^2_{on/off}\,\theta^2\chi^{-1}$ data. In i), lines are a fit to the equation $\frac{1}{T_1} = \frac{1}{T_{1,0mM}} + A[M]^{-B}$, where $T_{1,0mM}$ is the T_1 value of the undoped sample (see Table S1). All other lines are given as a guide to the eye. The raw data are given in Tables S5 and S6 in the Supporting Information. When error bars are smaller than the symbol, they are omitted.
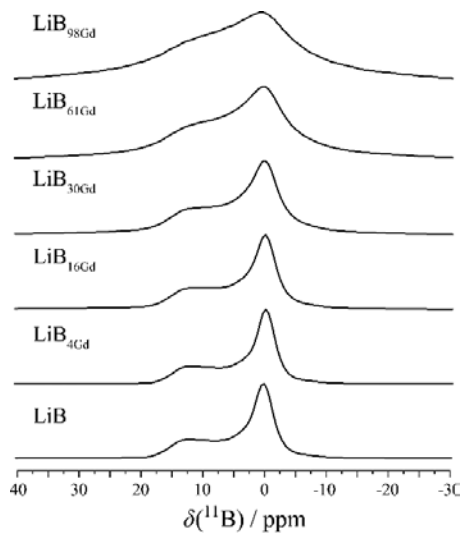
Figure 5. ^{11}B MAS NMR spectra of LiB glasses as a function of Gd^{3+} concentration. Highlighting the paramagnetic broadening of the quadrupolar features of the BO_3 environment. Spectra are normalized to their maximum intensities.

3.2.3. Zinc phosphate glasses. The ^{31}P DNP NMR results from the ZnP glasses (Figure 6) were consistent with those from the other systems. Briefly, Gd^{3+} again provided greater enhancements and time savings when compared to Mn^{2+}. Overall, the ^{31}P $\varepsilon_{on/off}$ values were modest, surpassing only those of ^{11}B. This is surprising, given that these glasses featured the second-longest T_1 values, and that ^{31}P has the largest gyromagnetic ratio of the nuclei studied and a 100% natural abundance. As such, we suspect that the structure around the metal ion has a large impact on how the polarization is transferred to the bulk.[49] Another possibility may be that the DNP enhancements are being diluted over the numerous ^{31}P spins.

The ^{31}P $\varepsilon_{on/off}^2 \theta^2 \chi^{-1}$ and $\varepsilon_{amp}^2 \chi^{-1}$ values were dramatically higher for the ^{31}P nuclei in the Gd^{3+}-doped ZnP series than for any other combination of dopants and nuclei, reaching a $\varepsilon_{on/off}^2 \theta^2 \chi^{-1}$ value of 550 ± 30. This tremendous time saving is predominantly driven by the nearly insignificant paramagnetic bleaching observed in this glass series, when compared to ^{29}Si (section 3.2.1), and the drastic reduction in T_1. For instance, at a dopant concentration of ~100 mM θ was of 0.69 in the Gd-doped ZnP glass while it was of 0.073 in for ^{29}Si in the Gd-doped LiSi glass. The ^{31}P NMR spectra also show increasing sideband patterns with increases in dopant concentration that can only be explained by the MAS-averaged hyperfine interaction (Figure S11). This averaging may also be responsible for the relatively low $\varepsilon_{on/off}$ values. These increases in sideband intensity were not observed in the other glasses since lower dopant concentrations were used.
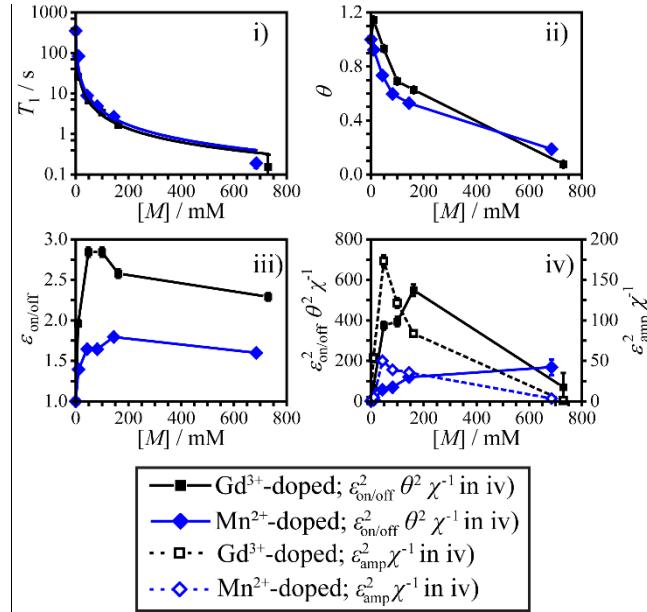

Figure 6. ZnP glasses: spin-lattice relaxation times T_1, contribution factors θ, DNP enhancements $\varepsilon_{on/off}$, integral time savings $\varepsilon_{on/off}^2 \theta^2 \chi^{-1}$, and vertical intensity time savings $\varepsilon_{amp}^2 \chi^{-1}$ for ^{31}P NMR. Data from Gd^{3+}-doped glasses are presented as black squares, while data from glasses doped with Mn^{2+} are presented as blue diamonds. In iv) the white-filled symbols and dashed lines correspond to the $\varepsilon_{amp}^2 \chi^{-1}$ values while the solid colors correspond to the $\varepsilon_{on/off}^2 \theta^2 \chi^{-1}$ data. In i), lines are a fit to the equation $\frac{1}{T_1} = \frac{1}{T_{1,0mM}} + A[M]^{-B}$, where $T_{1,0mM}$ is the T_1 value of the undoped sample (see Table S1). All other lines are given as a guide to

the eye. The raw data are given in Table S7 in the Supporting Information. When error bars are smaller than the symbol, they are omitted.

3.3. Gd^{3+} versus Mn^{2+}. A recurring observation in this study is that Gd^{3+} consistently outperformed Mn^{2+} as a polarization agent. The electronic and nuclear spin quantum numbers of the metals profoundly impact the efficiency of DNP.[28] Since we are using a monochromatic microwave source, we may only irradiate a single band of a hyperfine coupling pattern as well as only effectively saturate the sharpest $m = 1/2$ to $-1/2$ electronic transition. The electronic satellite transitions are not expected to play a significant role in the DNP process in either case due to their relative breadth.[27] Mn^{2+} has nuclear and electronic spin quantum numbers of 5/2 and as such only 1/3 of the paramagnetic centers are in the central electronic states and only 1/6 of these are coupled to ^{55}Mn in the given irradiated band. It follows that only 1/18 of the Mn^{2+} sites can participate in DNP. In comparison, 70% of Gd nuclei have nuclear spins of zero, with the two spin-3/2 isotopes (^{155}Gd and ^{157}Gd) having gyromagnetic ratios of roughly 1/6 that of ^{55}Mn. As such, the spin-specific losses in DNP efficiency for Gd^{3+} come predominantly from its electronic spin quantum number of 7/2, which reduces the DNP efficiency to 1/4. Note that at ultra-low temperatures the fraction of spins in the central states is further reduced due to Boltzmann effects but this effect is negligible at 100 K.[50] The differences in the fractions of spins that are efficiently irradiated is in agreement with the observed differences in DNP efficiency when using the two dopants.

4. Conclusions.

In summary, we investigated the utility of Gd^{3+} and Mn^{2+} as general polarization sources for MAS DNP experiments performed in inorganic materials using doped oxide glasses as proxies. Gd^{3+} consistently provided larger enhancements, yielding time savings on the order of 10 to 550. These time savings were, however, often accompanied by substantial line broadening and a loss of resolution. Although the efficacy of Gd^{3+} and Mn^{2+} doping in oxide glasses did not generally match that reported for bulk crystalline solids, the generality of this approach makes it attractive for the study of materials in which polarization cannot be transported via spin diffusion or for materials that do not generate radicals with favorable properties when γ-irradiated.

Supporting Information.

Plots and tabulated data for T_1, θ, $\varepsilon_{on/off}$, $\varepsilon^2_{on/off}$ $\theta^2\chi^{-1}$ and ε^2_{amp} χ^{-1} for all samples.

Author Information.

Corresponding Authors
*E-mail fperras@ameslab.gov
*E-mail mpruski@ameslab.gov
ORCID
Alexander L. Paterson: 0000-0002-3069-5910
Frédéric A. Perras: 0000-0002-2662-5119
Matthew F. Besser: 0000-0001-5721-3566
Marek Pruski: 0000-0001-7800-5336

Acknowledgements.

References.

[1] Rosay, M.; Tometich, L.; Pawsey, S.; Bader, R.; Schauwecker, R.; Blank, M.; Borchard, P. M.; Cauffman, S. R.; Felch, K. L.; Weber, R. T.; *et al*. Maas, W. E. Solid-State Dynamic Nuclear Polarization at 263 GHz: Spectrometer Design and Experimental Results. *Phys. Chem. Chem. Phys.* **2010**, *12*, 5850–5860.

[2] Maly, T.; Debelouchina, G. T.; Bajaj, V. S.; Hu, K.-N.; Joo, C.-G.; Mak-Jurkauskas, M. L.; Sirigiri, J. R.; van der Wel, P. C. A.; Herzfeld, J.; Temkin, R. J.; *et al*.Dynamic Nuclear Polarization at High Magnetic Fields. *J. Chem. Phys.* **2008**, *128*, 052211.

[3] Overhauser, A. W. Polarization of Nuclei in Metals. *Phys. Rev.* **1953**, *92*, 411–415.

[4] Lelli, M.; Gajan, D.; Lesage, A.; Caporini, M. A.; Vitzthum, V.; Miéville, P.; Héroguel, F.; Rascón, F.; Roussey, A.; Thieuleux, C.; *et al*. Fast Characterization of Functionalized Silica Materials by Silicon-29 Surface-Enhanced NMR Spectroscopy Using Dynamic Nuclear Polarization. *J. Am. Chem. Soc*. **2011**, *133*, 2104–2107.

[5] Lesage, A.; Lelli, M.; Gajan, D.; Caporini, M. A.; Vitzthum, V.; Miéville, P.; Alauzun, J.; Roussey, A.; Thieuleux, C.; Mehdi, A.; *et al*. Surface Enhanced NMR Spectroscopy by Dynamic Nuclear Polarization. *J. Am. Chem. Soc*. **2010**, *132*, 15459–15461.

[6] Conley, M. P.; Copéret, C.; Thieuleux, C. Mesostructured Hybrid Organic–Silica Materials: Ideal Supports for Well-Defined Heterogeneous Organometallic Catalysts. *ACS Catal.* **2014**, *4*, 1458–1469.

[7] Johnson, R. L.; Perras, F. A.; Kobayashi, T.; Schwartz, T. J.; Dumesic, J. A.; Shanks, B. H.; Pruski, M. Identifying Low-Coverage Surface Species on Supported Noble Metal Nanoparticle Catalysts by DNP-NMR. *Chem. Commun.* **2016**, *52*, 1859–1862.

[8] Leskes, M.; Kim, G.; Liu, T.; Michan, A. L.; Aussenac, F.; Dorffer, P.; Paul, S.; Grey, C. P. Surface-Sensitive NMR Detection of the Solid Electrolyte Interphase Layer on Reduced Graphene Oxide. *J. Phys. Chem. Lett*. **2017**, *8*, 1078–1085.

[9] Jin, Y.; Kneusels, N.-J. H.; Marbella, L. E.; Castillo-Martínez, E.; Magusin, P. C. M. M.; Weatherup, R. S.; Jónsson, E.; Liu, T.; Paul, S.; Grey, C. P. Understanding Fluoroethylene Carbonate and Vinylene Carbonate Based Electrolytes for Si Anodes in Lithium Ion Batteries with NMR Spectroscopy. *J. Am. Chem. Soc*. **2018**, *140*, 9854–9867.

[10] Protesescu, L.; Rossini, A. J.; Kriegner, D.; Valla, M.; de Kergommeaux, A.; Walter, M.; Kravchyk, K. V.; Nachtegaal, M.; Stangl, J.; Malaman, B.; *et al*. Unraveling the Core–Shell Structure of Ligand-Capped Sn/SnO$_x$ Nanoparticles by Surface-Enhanced Nuclear Magnetic Resonance, Mössbauer, and X-Ray Absorption Spectroscopies. *ACS Nano* **2014**, *8*, 2639–2648.

[11] Piveteau, L.; Ong, T.-C.; Walder, B. J.; Dirin, D. N.; Moscheni, D.; Schneider, B.; Bär, J.; Protesescu, L.; Masciocchi, N.; Guagliardi, A.; *et al*. Resolving the Core and the Surface of CdSe Quantum Dots and Nanoplatelets Using Dynamic Nuclear Polarization Enhanced PASS–PIETA NMR Spectroscopy. *ACS Cent. Sci*. **2018**, *4*, 1113–1125.

[12] Kobayashi, T.; Perras, F. A.; Slowing, I. I.; Sadow, A. D.; Pruski, M. Dynamic Nuclear Polarization Solid-State NMR in Heterogeneous Catalysis Research, *ACS Catal.* **2015**, *5*, 7055–7062.

[13] Lafon, O.; Rosay, M.; Aussenac, F.; Lu, X.; Trébosc, J.; Cristini, O.; Kinowski, C.; Touati, N.; Vezin, H.; Amoureux, J.-P. Beyond the Silica Surface by Direct Silicon-29 Dynamic Nuclear Polarization. *Angew. Chem., Int. Ed.* **2011**, *50*, 8367–8370.

[14] Brownbill, N. J.; Lee, D.; De Paëpe, G.; Blanc, F. Detection of the Surface of Crystalline Y_2O_3 Using Direct ^{89}Y Dynamic Nuclear Polarization. *J. Phys. Chem. Lett*. **2019**, *10*, 3501–3508.

[15] Rossini, A. J.; Zagdoun, A.; Hegner, F.; Schwarzwälder, M.; Gajan, D.; Copéret, C.; Lesage, A.; Emsley, L. Dynamic Nuclear Polarization NMR Spectroscopy of Microcrystalline Solids. *J. Am. Chem. Soc.* **2012**, *134*, 16899–16908.

[16] Pinon, A. C.; Schlagnitweit, J.; Berruyer, P.; Rossini, A. J.; Lelli, M.; Socie, E.; Tang, M.; Pham, T.; Lesage, A.; Schantz, S.; *et al*.Measuring Nano- to Microstructures from Relayed Dynamic Nuclear Polarization NMR. *J. Phys. Chem. C* **2017**, *121*, 15993–16005.

[17] Björgvinsdóttir, S.; Walder, B. J.; Pinon, A. C.; Emsley, L. Bulk Nuclear Hyperpolarization of Inorganic Solids by Relay from the Surface. *J. Am. Chem. Soc.* **2018**, *140*, 7946–7951.

[18] Björgvinsdóttir, S.; Walder, B. J.; Matthey, N.; Emsley, L. Maximizing Nuclear Hyperpolarization in Pulse Cooling Under MAS. *J. Magn. Reson.* **2019**, *300*, 142–148.

[19] Björgvinsdóttir, S.; Moutzouri, P.; Berruyer, P.; Hope, M. A.; Emsley, L. Sensitivity Enhancements in Lithium Titanates by Incipient Wetness Impregnation DNP NMR. *J. Phys. Chem. C* **2020**, *124*, 16524–16528.

[20] Katz, I.; Blank, A. Dynamic Nuclear Polarization in Solid Samples by Electrical-Discharge-Induced Radicals. *J. Magn. Reson.* **2015**, *261*, 95–100.

[21] Katz, I.; Feintuch, A.; Carmieli, R.; Blank, A. Proton Polarization Enhancement of Up to 150 with Dynamic Nuclear Polarization of Plasma-Treated Glucose Powder. *Solid State Nucl. Magn. Reson.* **2019**, *100*, 26–35.

[22] Carnahan, S. L.; Venkatesh, A.; Perras, F. A.; Wishart, J. F.; Rossini, A. J. High-Field Magic Angle Spinning Dynamic Nuclear Polarization Using Radicals Created by γ-Irradiation. *J. Phys. Chem. Lett.* **2019**, *10*, 4770–4776.

[23] Corzilius, B.; Michaelis, V. K.; Penzel, S. A.; Ravera, E.; Smith, A. A.; Luchinat, C.; Griffin, R. G. Dynamic Nuclear Polarization of ^{1}H, ^{13}C, and ^{59}Co in a Tris(ethylenediamine)cobalt(III) Crystalline Lattice Doped with Cr(III). *J. Am. Chem. Soc.* **2014**, *136*, 11716–11727.

[24] Kaushik, M.; Qi, M.; Godt, A.; Corzilius, B. Bis-Gadolinium Complexes for Solid Effect and Cross Effect Dynamic Nuclear Polarization. *Angew. Chem., Int. Ed.* **2017**, *56*, 4295–4299.

[25] Chakrabarty, T.; Goldin, N.; Feintuch, A.; Houben, L.; Leskes, M. Paramagnetic Metal-Ion Dopants as Polarization Agents for Dynamic Nuclear Polarization NMR Spectroscopy in Inorganic Solids. *ChemPhysChem* **2018**, *19*, 2139–2142.

[26] Kaushik, M.; Bahrenberg, T.; Can, T. V.; Caporini, M. A.; Silvers, R.; Heiliger, J.; Smith, A. A.; Schwalbe, H.; Griffin, R. G.; Corzilius, B. Gd(III) and Mn(II) Complexes for Dynamic Nuclear Polarization: Small Molecular Chelate Polarizing Agents and Applications with Site-Directed Spin Labeling of Proteins. *Phys. Chem. Chem. Phys.* **2016**, *18*, 27205–27218.

[27] Corzilius, B. Paramagnetic Metal Ions for Dynamic Nuclear Polarization. *eMagRes.* **2018**, *7*, 179–194.

[28] Corzilius, B.; Smith, A. A.; Barnes, A. B.; Luchinat, C.; Bertini, I.; Griffin, R. G. High-Field Dynamic Nuclear Polarization with High-Spin Transition Metal Ions. *J. Am. Chem. Soc.* **2011**, *133*, 5648–5651.

[29] Corzilius, B. Theory of Solid Effect and Cross Effect Dynamic Nuclear Polarization with Half-Integer High-Spin Metal Polarizing Agents in Rotating Solids. *Phys. Chem. Chem. Phys.* **2016**, *18*, 27190–27204.

[30] Wolf, T.; Kumar, S.; Singh, H.; Chakrabarty, T.; Aussenac, F.; Frenkel, A. I.; Major, D. T.; Leskes, M. Endogenous Dynamic Nuclear Polarization for Natural Abundance ^{17}O and Lithium NMR in the Bulk of Inorganic Solids. *J. Am. Chem. Soc*. **2019**, *141*, 451–462.

[31] Harchol, A.; Reuveni, G.; Ri, V.; Thomas, B.; Carmieli, R.; Herber, R. H.; Kim, C.; Leskes, M. Endogenous Dynamic Nuclear Polarization for Sensitivity Enhancement in Solid-State NMR of Electrode Materials. *J. Phys. Chem. C* **2020**, *124*, 7082–7090

[32] Jardon-Alvarez, D.; Reuveni, G.; Harchol, A.; Leskes, M. Enabling Natural Abundance ^{17}O Solid State NMR by Direct Polarization from Paramagnetic Metal Ions. *J. Phys. Chem. Lett.* **2020**, 11, 5439–5445.

[33] Stevanato, G.; Kubicki, D. J.; Menzildjian, G.; Chauvin, A.-S.; Keller, K.; Yulikov, M.; Jeschke, G.; Mazzanti, M.; Emsley, L. A Factor Two Improvement in High-Field Dynamic Nuclear Polarization from Gd(III) Complexes by Design. *J. Am. Chem. Soc*. **2019**, *141*, 8746–8751.

[34] Shermer, H. F. Thermal Expansion of Binary Alkali Silicate Glasses. *J. Res. Nat. Bur. Stand.* **1956**, *57*, 97–101.

[35] Shibata, M.; Sanchez, C.; Patel, H.; Feller, S.; Stark, J.; Sumcad, G.; Kasper, J. The Density of Lithium Borate Glasses Related to Atomic Arrangements. *J. Non-Cryst. Solids* **1986**, 85, 29–41.

[36] Suzuya, K.; Itoh, K.; Kajinami, A.; Loong, C.-K. The Structure of Binary Zinc Phosphate Glasses. *J. Non-Cryst. Solids* **2004**, *345-346*, 80–87.

[37] Blumberg, W. E. Nuclear Spin-Lattice Relaxation Caused by Paramagnetic Impuritites. *Phys. Rev.* **1960**, *119*, 79–84.

[38] Tse, D.; Lowe, I. J. Nuclear Spin-Lattice Relaxation in CaF$_2$ Crystals via Paramagnetic Centers. *Phys. Rev.* **1968**, *166*, 292–302.

[39] Bodart, J. R.; Bork, V. P.; Cull, T.; Ma, H.; Fedders, P. A.; Leopold, D. J.; Norberg, R. E. Recovery of Nuclear Magnetization Under Extreme Inhomogeneous Broadening. *Phys. Rev. B* **1996**, *54*, 15291–15298.

[40] Devreux, F.; Boilot, J. P.; Chaput, F.; Sapoval, B. NMR Determination of the Fractal Dimension in Silica Aerogels. *Phys. Rev. Lett.* **1990**, *65*, 614–617.

[41] Tse, D.; Hartmann, S. R.; Nuclear Spin-Lattice Relaxation Via Paramagnetic Centers Without Spin Diffusion. *Phys. Rev. Lett.* **1968**, *21*, 511–514.

[42] Schnauss, W.; Fujara, F.; Sillescu, H. The Molecular Dynamics Around the Glass Transition and in the Glassy State of Molecular Organic Systems: A ^{2}H-Nuclear Magnetic Resonance Study. *J. Chem. Phys.* **1992**, *97*, 1378–1389.

[43] Petrov, O. V.; Stapf, S. Parameterization of NMR Relaxation Curves in Terms of Logarithmic Moments of the Relaxation Time Distribution. *J. Magn. Reson.* **2017**, *279*, 29–38.

[44] Takahashi, H.; Lee, D.; Dubois, L.; Bardet, M.; Hediger, S.; De Paëpe, G. Rapid Natural-Abundance 2D ^{13}C–^{13}C Correlation Spectroscopy Using Dynamic Nuclear Polarization Enhanced Solid-State NMR and Matrix-Free Sample Preparation. *Angew. Chem., Int. Ed.* **2012**, *51*, 11766–11769.

[45] Thurber, K. R. and Tycko, R. Perturbation of Nuclear Spin Polarizations in Solid State NMR of Nitroxide-Doped Samples by Magic-Angle-Spinning Without Microwaves. *J. Chem. Phys.* **2014**, *140*, 184201.

[46] Mentink-Viger, F.; Paul, S.; Lee, D.; Feintuch, A.; Hediger, S.; Vega, S.; De Paëpe, G. Nuclear Depolarization and Absolute Sensitivity in Magic-Angle Spinning Cross Effect Dynamic Nuclear Polarization. *Phys. Chem. Chem. Phys.* **2015**, *17*, 21824–21836.

[47] Perras, F. A.; Wang, L.-L.; Manzano, J. S.; Chaudhary, U.; Opembe, N. N.; Johnson, D. D.; Slowing, I. I.; Pruski, M. Optimal Sample Formulations for DNP SENS: The Importance of Radical-Surface Interactions. *Curr. Opin. Colloid Interface Sci.* **2018**, *33*, 9–18.

[48] Hovav, Y.; Levinkron, O.; Feintuch, A.; Vega, S. Theoretical Aspects of Dynamic Nuclear Polarization in the Solid State: The Influence of High Radical Concentrations on the Solid Effect and Cross Effect Mechanisms. *Appl. Magn. Reson.* **2012**, *43*, 21–41.

[49] Perras, F. A.; Raju, M.; Carnahan, S. L.; Akbarian, D.; van Duin, A. C. T.; Rossini, A. J.; Pruski, M. Full-Scale Ab Initio Simulations of Magic-Angle-Spinning Dynamic Nuclear Polarization. *J. Phys. Chem. Lett.* **2020**, *11*, 5655–5660.

[50] Clayton, J. A.; Keller, K.; Qi, M.; Wegner, J.; Koch, V.; Hintz, H.; Godt, A.; Han, S.; Jeschke, G.; Sherwin, M. S.; Yulikov, M. Quantitative Analysis of Zero-Field Splitting Parameter Distributions in Gd(III) Complexes. *Phys. Chem. Chem. Phys.* **2018**, *20*, 10470–10492.